Delft University of Technology

High-Resolution Imaging of Intracellular Calcium Fluctuations Caused by Oscillating Microbubbles

Beekers, Inés; Mastik, Frits; Beurskens, Robert; Tang, Phoei Ying; Vegter, Merel; van der Steen, Antonius F.W.; de Jong, Nico; Verweij, Martin D.; Kooiman, Klazina

DOI
10.1016/j.ultrasmedbio.2020.03.029

Publication date
2020

Document Version
Final published version

Published in
Ultrasound in Medicine and Biology

Citation (APA)
Beekers, I., Mastik, F., Beurskens, R., Tang, P. Y., Vegter, M., van der Steen, A. F. W., de Jong, N., Verweij, M. D., & Kooiman, K. (2020). High-Resolution Imaging of Intracellular Calcium Fluctuations Caused by Oscillating Microbubbles. *Ultrasound in Medicine and Biology*, *46*(8), 2017-2029. https://doi.org/10.1016/j.ultrasmedbio.2020.03.029

Important note
To cite this publication, please use the final published version (if applicable).
Please check the document version above.

Copyright
Other than for strictly personal use, it is not permitted to download, forward or distribute the text or part of it, without the consent of the author(s) and/or copyright holder(s), unless the work is under an open content license such as Creative Commons.

Takedown policy
Please contact us and provide details if you believe this document breaches copyrights.
We will remove access to the work immediately and investigate your claim.

This work is downloaded from Delft University of Technology.
For technical reasons the number of authors shown on this cover page is limited to a maximum of 10.

Ultrasound in Med. & Biol., Vol. 46, No. 8, pp. 2017−2029, 2020
Copyright © 2020 The Author(s). Published by Elsevier Inc. on behalf of World Federation for Ultrasound in Medicine & Biology.
This is an open access article under the CC BY-NC-ND license. (http://creativecommons.org/licenses/by-nc-nd/4.0/)
Printed in the USA. All rights reserved.
0301-5629/$ - see front matter

https://doi.org/10.1016/j.ultrasmedbio.2020.03.029

● *Original Contribution*

HIGH-RESOLUTION IMAGING OF INTRACELLULAR CALCIUM FLUCTUATIONS CAUSED BY OSCILLATING MICROBUBBLES

INÉS BEEKERS,* FRITS MASTIK,* ROBERT BEURSKENS,* PHOEI YING TANG,* MEREL VEGTER,*
ANTONIUS F.W. VAN DER STEEN,*,† NICO DE JONG,*,† MARTIN D. VERWEIJ,*,† and KLAZINA KOOIMAN*
* Department of Biomedical Engineering, Thoraxcenter, Erasmus University Medical Center, Rotterdam, The Netherlands; and
† Laboratory of Acoustical Wavefield Imaging, Department of Imaging Physics, Delft University of Technology, Delft, The Netherlands

(*Received* 15 *January* 2020; *revised* 11 *March* 2020; *in final from* 26 *March* 2020)

Abstract—Ultrasound insonification of microbubbles can locally enhance drug delivery, but the microbubble−cell interaction remains poorly understood. Because intracellular calcium (Ca_i^{2+}) is a key cellular regulator, unraveling the Ca_i^{2+} fluctuations caused by an oscillating microbubble provides crucial insight into the underlying bio-effects. Therefore, we developed an optical imaging system at nanometer and nanosecond resolution that can resolve Ca_i^{2+} fluctuations and microbubble oscillations. Using this system, we clearly distinguished three Ca_i^{2+} uptake profiles upon sonoporation of endothelial cells, which strongly correlated with the microbubble oscillation amplitude, severity of sonoporation and opening of cell−cell contacts. We found a narrow operating range for viable drug delivery without lethal cell damage. Moreover, adjacent cells were affected by a calcium wave propagating at 15 μm/s. With the unique optical system, we unraveled the microbubble oscillation behavior required for drug delivery and Ca_i^{2+} fluctuations, providing new insight into the microbubble−cell interaction to aid clinical translation. (E-mail addresses: d.beekers@erasmusmc.nl, k.kooiman@erasmusmc.nl) © 2020 The Author(s). Published by Elsevier Inc. on behalf of World Federation for Ultrasound in Medicine & Biology. This is an open access article under the CC BY-NC-ND license. (http://creativecommons.org/licenses/by-nc-nd/4.0/).

Key Words: **Drug delivery, Microbubbles, Ultrasound, Intracellular calcium, Sonoporation, Cell−cell contact opening, Confocal microscopy, High-speed imaging.**

INTRODUCTION

Effective disease treatment depends largely on the ability of drugs to overcome barriers imposed by the human body to reach the diseased tissue. The blood−brain barrier is almost impermeable to drugs, blocking an estimated ~98% of small molecule drugs, posing a major challenge in the treatment of neurological disorders (Neuwelt et al. 2008). Limited drug delivery is also observed—to a lesser extent—in other tissues; for example, chemotherapy drugs need to extravasate blood vessels and migrate through the extravascular space to reach the tumor (Mullick Chowdhury et al. 2017; Yang et al. 2019). All in all, the vascular endothelium forms a major barrier to localized drug delivery. Consequently, higher drug dosages are prescribed to reach the proper efficacy level but this results in high systemic toxicity and development of side effects. Therefore, there is a need for a novel method to facilitate efficient drug delivery to diseased tissues and thereby minimize adverse effects.

Vascular drug delivery can be locally enhanced by ultrasound insonification of lipid-coated microbubbles (1−10 μm in diameter) (Bao et al. 1997; Miller et al. 1999; Wu and Nyborg 2008; Sutton et al. 2013; Kooiman et al. 2014). These microbubbles are widely used in the clinic to improve contrast in diagnostic ultrasound imaging and additionally have a therapeutic potential. Upon insonification, microbubbles will oscillate and can thereby stimulate the following drug delivery pathways: perforate the cell membrane (*i.e.,* sonoporation), open intercellular junctions and stimulate endocytosis (Kooiman et al. 2014; Lentacker et al. 2014; Qin et al. 2018b; Roovers et al. 2019). Moreover, oscillating microbubbles can induce intracellular calcium (Ca_i^{2+}) fluctuations (Honda et al. 2004; Kumon et al. 2007, 2009; Juffermans et al. 2006, 2009; Meijering et al. 2009; Fan et al. 2010; Park et al. 2011), which can propagate to adjacent cells within seconds through intercellular signaling mechanisms, causing calcium waves (Leybaert and Sanderson

---

Address correspondence to: Inés Beekers, Office Ee2302, PO Box 2040, 3000CA Rotterdam, The Netherlands. E-mail addresses: d.beekers@erasmusmc.nl, k.kooiman@erasmusmc.nl

2012). As Ca_i^{2+} plays a crucial role in junction integrity, membrane resealing and intercellular signaling, different Ca_i^{2+} fluctuations and recovery profiles correlate to post-treatment cell viability (Deng et al. 2004; Mehta and Malik 2006; Hassan et al. 2010).

A better understanding of when cell viability is preserved in microbubble-mediated drug delivery is required to control the balance between high delivery efficiency and lethal cell damage, and tune this to the requirements of a therapeutic application. Thus far, the specific microbubble−cell interaction necessary for the distinct drug delivery pathways, Ca_i^{2+} fluctuations and calcium waves remains poorly understood (Qin et al. 2018b). Elucidating the effect of an oscillating microbubble on Ca_i^{2+} levels will help unravel the underlying physical and biological mechanisms of microbubble-mediated drug delivery, including the potential downstream biological pathways triggered upon altering Ca_i^{2+} homeostasis. A better understanding of the therapeutic potential of microbubbles will aid development toward safe and efficient widespread clinical use.

To date, the microbubble−cell interaction causing Ca_i^{2+} fluctuations has been investigated while focusing on the cellular response. These studies have found that Ca_i^{2+} fluctuations induced by oscillating microbubbles can remain elevated (Kumon et al. 2007, 2009) or return to equilibrium within approximately 180 s (Juffermans et al. 2006, 2009; Meijering et al. 2009; Fan et al. 2010; Hassan et al. 2010; Park et al. 2011). Additionally, these Ca_i^{2+} fluctuations can propagate to adjacent cells via calcium waves, both by means of internal messengers through gap junctions and/or by paracrine signaling through the extracellular space (Leybaert and Sanderson 2012). This intercellular communication can also occur due to an oscillating microbubble, resulting in the delayed Ca_i^{2+} transients in adjacent cells that have been observed in rat cardiomyoblasts (Fan et al. 2010), Chinese hamster ovary cells (Kumon et al. 2007, 2009) and endothelial cells (Park et al. 2011).

It remains poorly understood how the spatiotemporal Ca_i^{2+} fluctuations correlate with microbubble oscillation behavior and the different drug delivery pathways. Only for Ca_i^{2+} fluctuations returning to equilibrium has the change in Ca_i^{2+} upon sonoporation been found to positively correlate with the final amount of propidium iodide (PI) uptake upon sonoporation, as observed in rat cardiomyoblasts (Fan et al. 2010). In human endothelial cells, microbubble-induced Ca_i^{2+} fluctuations have been reported (Juffermans et al. 2009; Park et al. 2011), but lacking information on single-cell response, microbubble location and behavior and a direct correlation with sonoporation. Additionally, the observed Ca_i^{2+} fluctuations always returned to equilibrium within ~180 s, and calcium waves were only shown for a single example, without further quantification. At present, it remains unknown how the spatiotemporal behavior of Ca_i^{2+} fluctuations relates to microbubble-mediated opening of cell−cell contacts. Live cell microscopy imaging of cell−cell contact opening by an oscillating microbubble has only been reported once before in the literature, for a single example and without Ca_i^{2+} imaging (Helfield et al. 2016). None of the previous studies were able to resolve the specific microbubble oscillation that induced the Ca_i^{2+} fluctuations, and therefore, the microbubble-cell interaction was never fully elucidated. Moreover, microbubble-induced Ca_i^{2+} fluctuations have only been imaged at low spatial resolution (widefield microscopy) and at a temporal resolution up to 1.7 frames/s (fps) (Kumon et al. 2009), such that calcium wave propagation was poorly resolved.

To unravel the microbubble−cell interaction mechanisms, we developed a novel optical imaging system consisting of the Brandaris 128 ultra-high-speed camera, to image microbubble oscillation at nanosecond temporal resolution, coupled to a custom-built Nikon A1R+ confocal microscope, to resolve cellular response at nanometer spatial resolution. The endothelial cell response upon insonification of a single targeted microbubble was evaluated by monitoring the spatiotemporal fluctuations of Ca_i^{2+}, uptake of PI as a marker for sonoporation and opening of cell−cell contacts. As a result, the microbubble−cell interaction was studied at both nanosecond and nanometer resolution.

METHODS

Endothelial cell culture

Pooled primary human umbilical vein endothelial cells (HUVECs; C2519A, LOT437550, Lonza, Verviers, Belgium) were cultured in MV2 medium (C22121, PromoCell GmbH, Heidelberg, Germany), supplemented with 1% penicillin−streptomycin (15140122, Gibco, Thermo Fisher Scientific, Waltham, MA, USA). The HUVECs were grown to full confluency in T75 flasks (at 37°C and 5% CO_2) in a humidified incubator before detaching them using Accutase solution (A6964, Sigma-Aldrich, St. Louis, MO, USA). The cells were then plated into acoustically characterized CLINIcells (membrane thickness 50 μm; CLINIcell25-50-T, Mabio, Tourcoing, France) (Beekers et al. 2019b) and grown for two days into a fully confluent cell monolayer. The medium was refreshed the day after plating. In total, 14 CLINIcells were cultured for experiments with ultrasound and microbubbles, 4 CLINIcells for ultrasound-only experiments (*i.e.,* without microbubbles), 3 CLINIcells for sham experiments (*i.e.,* without microbubbles or ultrasound) and 1 CLINIcell for the $\alpha_v\beta_3$-targeted microbubble specificity experiment described below.

Microbubble preparation

Lipid-coated microbubbles with a C_4F_{10} gas core were made by 1-min probe sonication, as described previously (Klibanov et al. 2004). The coating consisted of 1,2-distearoyl-*sn*-glycero-3-phosphocholine (DSPC, 84.8 mol%, P6517, Sigma-Aldrich); polyoxyethylene-40-stearate (PEG-40 stearate, 8.2 mol%, P3440, Sigma-Aldrich); 1,2-distearoyl-*sn*-glycero-3-phosphoethanolamine-*N*-[carboxy(polyethylene glycol)-2000] (DSPE-PEG(2000), 5.9 mol%, PEG6175.0001, Iris Biotech GmbH, Marktredwitz, Germany); and 1,2-distearoyl-*sn*-glycero-3-phosphoethanolamine-*N*-[biotinyl(polyethylene glycol)-2000] (DSPE-PEG(2000)-biotin, 1.1 mol%, 880129C, Avanti Polar Lipids, Alabaster, AL, USA). Next, microbubbles were washed three times by centrifugation (400*g*, 1 min) and counted with a Coulter Counter Multisizer 3 (20-μm aperture tube, Beckman Coulter, Mijdrecht, Netherlands). To target the microbubbles to the integrin $\alpha_v\beta_3$ (also known as CD51/61), they were functionalized using biotin−streptavidin bridging (Lindner et al. 2001). Briefly, 6×10^8 microbubbles were incubated on ice for 30 min with 60 μg streptavidin (S4762, Sigma-Aldrich), washed once, incubated on ice for 30 min with 6 μg of biotinylated anti-human CD51/61 antibody (304412, BioLegend, San Diego, CA, USA) and washed once again. Control microbubbles were produced by substituting the CD51/61 antibody for its biotinylated isotype control (2600520, Sony Biotechnology, San Jose, CA, USA).

$\alpha_v\beta_3$-targeting specificity assays

Expression of $\alpha_v\beta_3$ by HUVECs was evaluated with the following immunohistochemistry assay. The cells cultured in a CLINIcell were fixated for 20 min with 4% formaldehyde, washed three times with phosphate-buffered saline and blocked for 30 min with 5% goat serum (G6767, Sigma-Aldrich). After the blocking solution was removed, 2 × 3 cm pieces were cut from the CLINIcell membrane with cells. These pieces were incubated overnight at 4°C with primary antibody biotinylated anti-human CD51/61 (diluted 1:100, 304412, BioLegend). After washing with 0.5% Tween-20, we blocked again for 30 min with 5% goat serum. Next, the HUVECs were incubated for 60 min with secondary antibody anti-mouse Alexa Fluor 488 (diluted 1:100, A-11029, Thermo Fisher Scientific), washed three times with 0.5% Tween-20 and incubated for 5 min with Hoechst 33342 (5 μg/mL final concentration, H3570,

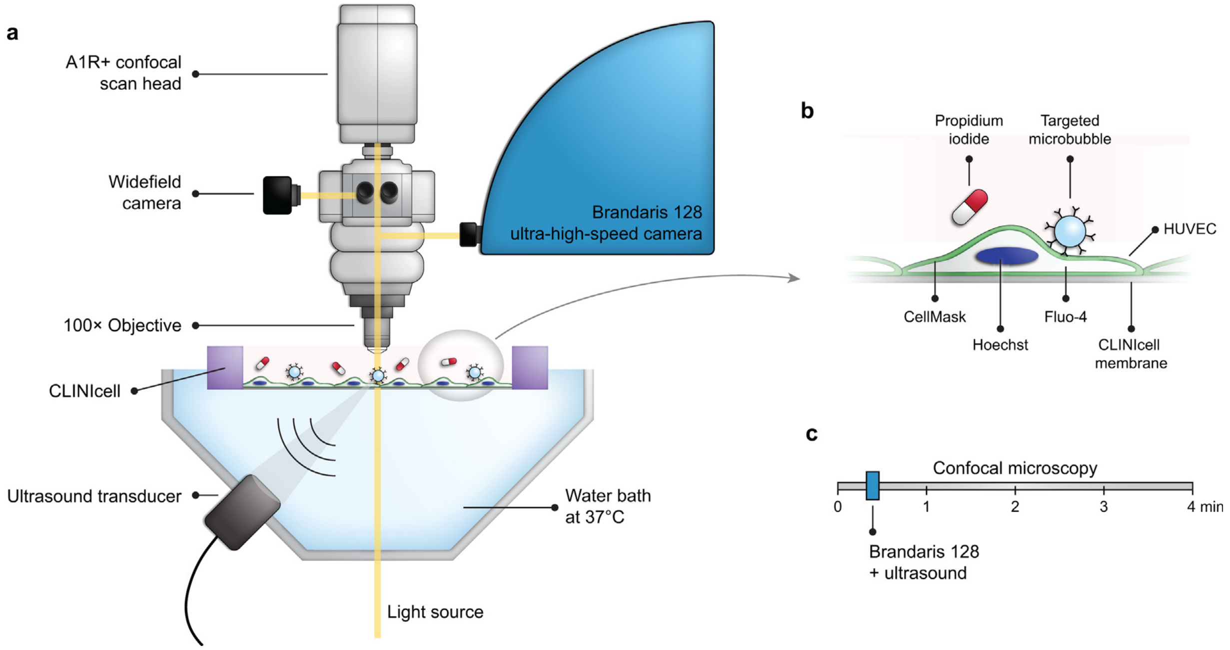

Fig. 1. Schematic of the experimental setup (not drawn to scale). (a) The optical imaging system consisted of the Brandaris 128 ultra-high-speed camera, an A1R+ confocal microscope and a DS-Fi3 (Nikon Instruments) color camera for widefield imaging. HUVECs were cultured on the bottom membrane of a CLINIcell, and the top membrane was removed just before inserting the CLINIcell in the water bath at 37°C. Ultrasound insonification occurred under a 45° angle, after alignment of the ultrasound and optical foci. (b) The HUVEC nuclei were stained with Hoechst (pseudo-colored in *blue*), the cell membranes with CellMask Deep Red (pseudo-colored in *green*) and the intracellular calcium with Fluo-4 (pseudo-colored in *white*). Propidium iodide (pseudo-colored in *red*) was added to the medium as a marker for sonoporation. The $\alpha_v\beta_3$-targeted microbubbles were bound to the HUVECs. (c) Timeline of the imaging procedure with the combined optical imaging system and ultrasound insonification. HUVEC = human umbilical vein endothelial cells.

Thermo Fisher Scientific) to stain the cell nuclei. The samples were mounted on a microscope slide in 100 μL of Vectashield Hardset (H-1400, Vector Laboratories, Burlingame, CA, USA). Specificity of the primary antibody CD51/61 was assessed by substituting the antibody for the biotinylated IgG1-κ isotype control (diluted 1:100, 2600520, Sony Biotechnology). The expression was visualized with confocal microscopy (60 × objective, A1R+, Nikon Instruments, Amsterdam, Netherlands). Finally, microbubble targeting specificity was also assessed by adding either $\alpha_v\beta_3$ -targeted microbubbles or control microbubbles to a CLINIcell (2×10^6 microbubbles/mL) and counting the number of microbubbles bound to the live HUVECs in 20 different fields of view (202 × 143 μm) using brightfield microscopy imaging and a 60 × water dipping objective (CFI Plan Apochromat VC 60XC WI, Nikon Instruments).

Experimental setup

Figure 1 is a schematic of the developed optical imaging system, consisting of the Brandaris 128 ultra-high-speed camera (Chin et al. 2003) (up to 25 million frames per second [Mfps]) coupled to a custom-built Nikon A1R+ confocal microscope (Beekers et al. 2019a). The integrated experimental setup for simultaneous imaging and ultrasound insonification is also illustrated in Figure 1, which illustrates HUVECs cultured on the bottom membrane of a CLINIcell, placed in a water bath at 37°C and insonified from below. A single-element focused transducer (2.25-MHz center frequency, 76.2-mm focal length, −6-dB beam width at 2 MHz of 3 mm, V305, Panametrics-NDT, Olympus) was mounted in the water bath at a 45° angle, to avoid standing wave buildup. The transducer output was calibrated in a separate experiment using a needle hydrophone (1-mm diameter, PA2293, Precision Acoustics, Dorchester, UK). The ultrasound and optical foci were aligned using a pulse-echo approach and a needle tip located at the optical focal plane (Chen et al. 2013). A single 2-MHz and 10-cycle burst was generated by an arbitrary waveform generator (33220A, Agilent, Palo Alto, CA, USA). A broadband amplifier (ENI A-500, Electronics & Innovation, Rochester, NY, USA) was used to obtain peak negative pressures of 100, 250 and 400 kPa. These ultrasound settings (mechanical index <0.3) were chosen to cause stable cavitation, while avoiding jetting and buildup of acoustic streaming. By use of a 100 × water dipping objective (CFI Plan 100XC W, 2.5-mm working distance, Nikon Instruments), a field of view of 128 × 128 μm (512 × 512 pixels, 0.25 μm/pixel) was imaged at 5 fps with the confocal microscopy resonant scanner. The system can automatically switch between confocal microscopy and Brandaris 128 ultra-high-speed imaging by triggering a motorized turret to rotate a full mirror into and out of the light path.

Live cell experimental protocol

For live confocal microscopy imaging, the HUVECs were stained with fluorescent dyes, while remaining in the MV2 culture medium. First, the cells were incubated for 10 min with 4 μg/mL CellMask Deep Red (C10046, Thermo Fisher Scientific) to stain the cell membrane and 1.8 μM Fluo-4 (F14201, Invitrogen, Carlsbad, CA, USA) to evaluate the intracellular calcium (Ca_i^{2+}) concentration. Then the cells were incubated for 5 min with 2×10^5 microbubbles/mL, 5 μg/mL Hoechst 33342 to stain the nuclei and 25 μg/mL PI (P4864, Sigma-Aldrich) as a marker for sonoporation. The cell membrane of viable cells is impermeable to PI. When the cell membrane is compromised, PI enters the cell, binds to DNA and RNA and becomes fluorescent (Edidin 1970). Therefore, PI is often used as a marker for sonoporation to evaluate membrane perforation (van Wamel et al. 2006; Fan et al. 2012; Shamout et al. 2015; Helfield et al. 2016; van Rooij et al. 2016; Qin et al. 2018a; Wang et al. 2018; Juang et al. 2019). During the last incubation step, the CLINIcell was turned upside down to allow the targeted microbubbles to float toward the cells to achieve binding. Subsequently, the CLINIcell was turned upright again, such that only the bound targeted microbubbles remained in the focal plane of the cells. The top membrane without cells was cut from the CLINIcell to image with the 100 × objective from above. In sham (*i.e.,* without microbubbles and ultrasound) and ultrasound-only (*i.e.,* without microbubbles) experiments the same incubation timeline was used, but without adding microbubbles. In each CLINIcell, a maximum of 15 locations spaced by at least 1 cm were imaged within 2 h. At each location, there was only one single targeted microbubble in the field of view. In addition, this targeted microbubble was located on a cell that was completely within the field of view, and this cell had a single nucleus that did not overlap with neighboring cells. Confocal microscopy time-lapse imaging was performed during 4 min using the following four channels: (i) Hoechst excited at 405 nm, detected at 450/50 nm (center wavelength/bandwidth), pseudo-colored in blue; (ii) Fluo-4 excited at 488 nm, detected at 525/50 nm, pseudo-colored in white; (iii) PI excited at 561 nm, detected at 595/50 nm, pseudo-colored in red; and (iv) CellMask Deep Red excited at 640 nm, detected at 700/70 nm, pseudo-colored in green. Channels 1 and 4 were imaged simultaneously as there was no spectral overlap. Imaging started before insonification to visualize the initial cell state. Then, the system automatically switched to the Brandaris 128 ultra-high-speed camera to record microbubble oscillation during insonification at ∼17

Mfps under brightfield illumination. Once this acquisition was completed, confocal microscopy time-lapse imaging was automatically restored within 500 ms after the Brandaris 128 acquisition to observe the local cellular response during >210 s.

Brandaris 128 image processing

Microbubble oscillation was quantified using custom-designed image analysis software to determine the change in radius as a function of time (van der Meer et al. 2007). Microbubble oscillation amplitude was defined as the difference between the maximum radius (R_{max}) and the initial radius (R_0, determined from the first 10 frames without ultrasound). The oscillation amplitude thresholds for sonoporation and irreversible Ca_i^{2+} fluctuations were determined by linear discriminant analysis (Helfield et al. 2016).

Confocal microscopy image analysis

The cellular response after ultrasound was evaluated for sonoporation, opening of cell−cell contacts and Ca_i^{2+} fluctuations. First, when the PI intensity increased upon insonification, the cell was classified as sonoporated. Second, when the CellMask signal exhibited a gap forming between the cell and its neighbor(s), the cell was classified as undergoing opening of cell−cell contacts. Finally, changes in Fluo-4 intensity in the cell were evaluated to classify Ca_i^{2+} fluctuations as described below. To quantitatively assess the local cellular response, custom-built image analysis software was used to manually register the microbubble location and delineate the cell with the targeted microbubble and all its adjacent neighbors. In case of opening of cell−cell contacts, the cell delineation was adjusted as a function of time to account for cell movement. All analyses were performed with MATLAB (The MathWorks, Natick, MA, USA).

Quantification of sonoporation

Sonoporation was quantified by the amount of PI uptake to determine the pore size and resealing properties, as mathematically described by Fan et al. (2012). Fluorescence intensity $F(t)$ was defined as the sum of PI fluorescence intensity of all the pixels within the delineated cell area after ultrasound minus mean PI fluorescence intensity before ultrasound. By use of a non-linear least-squares approach in MATLAB, $F(t)$ was fitted to

$$F(t) = \frac{\alpha}{\beta}\left(1 - e^{-\beta t}\right) \tag{1}$$

where α is the pore size coefficient, and β is the pore resealing coefficient. $F(t)$ reaches an asymptotic value when PI uptake stabilizes, caused by pore resealing. The sonoporated cells were classified as previously described by van Rooij et al. (2016). Briefly, when 90% of the asymptotic value of $F(t)$ was reached in less than 120 s or not, the sonoporated cells were classified as resealing <120 s or non-resealing, respectively. Cells that resealed within 120 s were additionally classified using principal component analysis into low PI, with small pore sizes and high pore resealing coefficients, and high PI, with large pore sizes and low pore resealing coefficients. Large pores that reseal insufficiently will cause more severe cell damage. To quantify this severity of sonoporation, a pore damage coefficient was defined as the ratio between the pore size coefficient (α) and the pore resealing coefficient (β).

Quantification of intracellular calcium (Ca_i^{2+}) fluctuations

The Ca_i^{2+} fluctuations were quantified based on the relative Ca_i^{2+} level, defined as the mean Fluo-4 fluorescence intensity after ultrasound normalized to the mean Fluo-4 fluorescence intensity before ultrasound, within the delineated cell area. The noise level for Ca_i^{2+} fluctuations was determined from the maximum relative Ca_i^{2+} level in control experiments (sham and ultrasound only). We found that the Fluo-4 intensity could increase up to an average of 30% in control experiments, because of, for instance, changes in cell loading or shifting of the focal plane. To quantitatively assess the cellular response, a Ca_i^{2+} fluctuation was defined as an increase in the Fluo-4 fluorescence intensity by more than 60% (twice the noise level) during at least 2 s. This corresponds to a relative Ca_i^{2+} level >1.6. This quantification led to the following four classes of Ca_i^{2+} fluctuations: (i) “stable” when the relative Ca_i^{2+} level did not increase above the 1.6 threshold during 2 s; (ii) “<180 s” when the relative Ca_i^{2+} level increased above 1.6 during 2 s and decreased below this threshold within 180 s; (iii) “>180 s” when the relative Ca_i^{2+} level increased above 1.6 during 2 s and remained above this threshold after 180 s; and (iv) “clusters” when the relative Ca_i^{2+} level increased above 1.6 during 2 s, then quickly dropped, leaving only a granular-like fluorescence pattern of Ca_i^{2+}.

Quantification of calcium waves

To determine if a calcium wave was induced upon sonoporation, the relative Ca_i^{2+} level in the adjacent cells was monitored in fields of view with a single sonoporated cell ($n = 55$). When the relative Ca_i^{2+} level in an adjacent cell was >1.6 during at least 2 s, this cell was labeled as affected. The fraction of affected cells in a calcium wave is a measure of the extent of disturbance caused by the wave, and was defined as the ratio between the number of affected adjacent cells and the total number of adjacent cells. Next, to quantify the speed at which the calcium wave propagated toward adjacent cells, we considered it a spherical wave propagating outward from its origin at the microbubble location. To do so, the field of view was converted to a spherical coordinate system centered at the microbubble and segmented into radial bands of 1 μm. On average, the field of view was split up in 59 radial bands. The mean relative Ca_i^{2+} level in each radial band was determined for each time frame. This allowed us to quantify the calcium wave propagation in color-coded maps as a function of time and distance from the microbubble. In each radial band, the wavefront arrival time was defined as the time at which the relative Ca_i^{2+} level was >1.6 and then remained elevated for at least 2 s. The slope of the linear fit through those arrival times was defined as the calcium wavefront speed. Additionally, we evaluated the propagation of Ca_i^{2+} within each adjacent cell. As before, the spherical coordinate system centered at the microbubble was used to partition the field of view into radial bands of 1 μm. However, now the cell delineation of each adjacent cell was used to mask these radial bands. The mean relative Ca_i^{2+} levels in the masked radial bands were determined for each time frame. This resulted in a color-coded map as a function of time and distance from the microbubble for each adjacent cell. The wavefront arrival times were again determined, and the calcium wavefront speed within each cell was obtained. See Supplementary Figure S1 (online only) for a stepwise example of this method.

Statistical analysis

Categorical data were tested for significant differences using Pearson's χ^2-test. Quantitative data (microbubble oscillation amplitude, pore damage coefficient, fraction of affected cells and calcium wavefront speed) were not normally distributed and thus were expressed as median and interquartile ranges. To test for significant differences, the two-sided Mann–Whitney *U*-test was performed. Statistically significant differences were indicated in the graphs with asterisks. All boxplots were presented with the central line at the median, the box limits at the first and third quartiles and the whiskers ranging from the minimum to the maximum value. Spearman's rank-order correlation was performed to determine the relationship between the microbubble oscillation amplitude and the fraction of affected cells in a calcium wave. All statistical analyses were performed with MATLAB.

RESULTS

Cellular response to a single oscillating microbubble

The cellular response to a single $\alpha_v\beta_3$-targeted microbubble (Supplementary Fig. 2, online only) upon

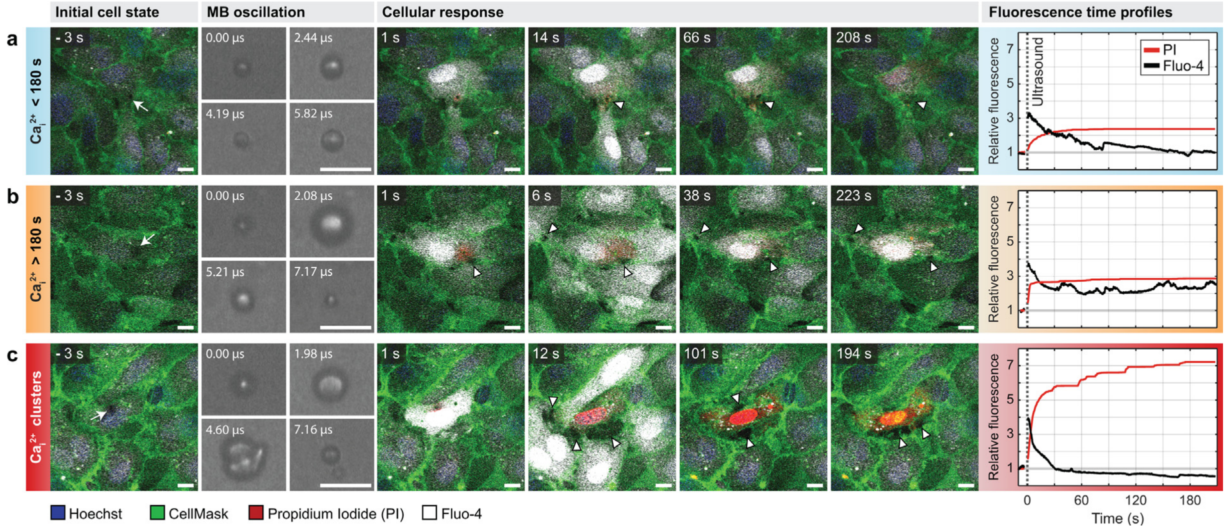

Fig. 2. Combined Brandaris 128 ultra-high-speed imaging and confocal microscopy. Selected frames of Brandaris 128 imaging and confocal microscopy time-lapse imaging illustrating a single oscillating targeted microbubble (MB) that induced sonoporation, opening of cell-cell contacts (indicated by *white triangles*) and intracellular calcium (Ca_i^{2+}) fluctuations. The Ca_i^{2+} fluctuations either (a) remained elevated <180 s, (b) remained elevated >180 s or (c) resulted in a clustered pattern of Ca_i^{2+}. The fluorescence intensity of propidium iodide (PI) and Fluo-4 relative to that before ultrasound is illustrated in the panels on the bottom. Cell nuclei in *blue*, cell membrane in *green*, PI in *red* and Ca_i^{2+} in *white*. The microbubble location was indicated with an *arrow* in the initial cell state. Bars = 10 μm. The corresponding confocal microscopy recordings can be found in Supplementary Videos 1, 2 and 3. To better distinguish PI uptake, see Supplementary Figure S3 for the red channel of confocal microscopy imaging. Radius–time curves of the respective microbubble oscillation can be found in Supplementary Figure S4, and a more detailed image of the clustered pattern can be found in Supplementary Figure S5.

ultrasound insonification was evaluated (n = 108). Selected frames of confocal microscopy and Brandaris 128 imaging are presented in Figure 2, illustrating three distinct cellular responses caused by an oscillating microbubble. The corresponding confocal microscopy recordings can be found in Supplementary Videos S1, S2 and S3 (online only). To better distinguish PI uptake upon sonoporation, the red channel of these confocal microscopy frames is provided in Supplementary Figure S3 (online only). Before ultrasound, a single targeted microbubble (*arrow,* Fig. 2) was bound to the central cell in each field of view. Confocal microscopy imaging of the initial cellular state revealed that all cells were viable and had an intact cell membrane, indicated by the absence of PI (*red channel,* in Fig. 2 and Supplementary Fig. S3, online only). There was a similar equilibrium level of Ca_i^{2+} in all cells, as indicated by the overall Fluo-4 signal (*white channel,* Fig. 2). Next, the microbubble oscillation was recorded with the Brandaris 128 ultra-high-speed camera during ultrasound and quantified as illustrated in Supplementary Figure S4 (online only). All microbubbles remained bound to the cells during oscillation, as they were still in the same focal plane after ultrasound. After ultrasound, PI uptake (*red channel,* Fig. 2 and Supplementary Figure S3, online only) was observed locally around the microbubble location and then diffused throughout the cell, indicative of sonoporation. The time profiles of the PI intensity upon sonoporation were determined based on the red fluorescent intensity within the cell, normalized to that before ultrasound (panels on the right of Fig. 2). The PI intensity was highest in Figure 2c, suggesting that more of this fluorescent marker was able to enter the cell through the pore created in the cell membrane than in Figure 2a and 2b. Additionally, upon PI influx, there was a simultaneous increase in Fluo-4 intensity (*white channel,* Fig. 2) in the sonoporated cell. Successively, the Fluo-4 intensity also increased in adjacent non-sonoporated cells, which is described in more detail in the section Calcium Waves. Three distinct Ca_i^{2+} fluctuations were observed in the sonoporated cells: (i) Ca_i^{2+} increased upon sonoporation and remained elevated <180 s, after which it returned to the initial Ca_i^{2+} level (Fig. 2a); (ii) Ca_i^{2+} increased upon sonoporation but did not return to the initial Ca_i^{2+} level within 180 s (Fig. 2b); (iii) Ca_i^{2+} increased upon sonoporation but quickly decreased and only a clustered pattern of Ca_i^{2+} remained (Fig. 2c and Supplementary Fig. S5, online only). A high-resolution image of a typical clustered Ca_i^{2+} pattern can be found in Supplementary Figure S5. For each of the Ca_i^{2+} fluctuations, the time profiles of the Fluo-4 intensity are shown in the panels on the right in Figure 2. Finally, the CellMask imaging (*green channel,* Fig. 2) revealed changes in border integrity as gaps (*arrowheads,* Fig. 2) formed between the sonoporated cell and its neighbors, indicative of cell−cell contact opening. Overall, the cellular response upon ultrasound insonification of a microbubble was studied in 108 fields of view.

Intracellular calcium fluctuations upon sonoporation

The oscillating microbubble caused sonoporation in 71% of the cells (77 of 108 cells) and sonoporation always resulted in a local increase in Ca_i^{2+} (77 of 77 cells, Fig. 3a). When the oscillating microbubble caused no sonoporation, it never induced a local increase in Ca_i^{2+} (n = 31, Fig. 3a). An increase in Ca_i^{2+} occurs upon pore formation caused by a concentration imbalance, as the free calcium concentration is about 10,000-fold lower in the cytosol than outside the cell (Carafoli and Krebs 2016). Depending on the temporal evolution of the Ca_i^{2+} increase upon sonoporation, the Ca_i^{2+} fluctuations were categorized in the three distinct responses illustrated in Figure 2. In 19% of the sonoporated cells, the Ca_i^{2+} level was elevated <180 s (n = 15), in 49% of

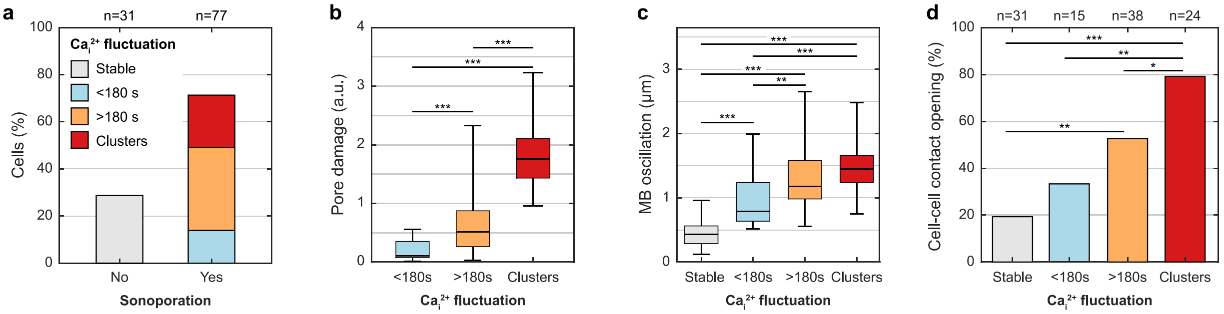

Fig. 3. Intracellular calcium (Ca_i^{2+}) fluctuations upon sonoporation and cell−cell contact opening. (a) Occurrence of sonoporation and the distinct Ca_i^{2+} fluctuations upon an oscillating microbubble. (b) Pore damage upon sonoporation for each class of Ca_i^{2+} fluctuations. (c) Microbubble oscillation amplitude for each class of Ca_i^{2+} fluctuation. (d) Occurrence of cell−cell contact opening upon different Ca_i^{2+} fluctuations. Boxplots illustrate the median and interquartile range; the whiskers extend from minimum value to maximum value. Statistically significant differences: $*p < 0.05$, $**p < 0.01$, $***p < 0.001$.

the cells $\mathrm{Ca_i^{2+}}$ was elevated >180 s (n = 38) and in 31% of the cells $\mathrm{Ca_i^{2+}}$ exhibited clusters (n = 24). Sonoporation was never observed in sham (n = 36) or ultrasound-only control experiments (n = 15 at 100 kPa, n = 15 at 250 kPa, n = 14 at 400 kPa). When there was no sonoporation, in only 1.6% of the monitored cells there was a spontaneous increase in $\mathrm{Ca_i^{2+}}$ levels that returned to equilibrium within 180 s (3 of 216 cells for sham and 5 of 264 cells for ultrasound only).

For each sonoporated cell, the pore size and pore resealing coefficients are given in Supplementary Figure S6 (online only). When the pore created upon sonoporation was small and resealed within 120 s (low PI uptake), the $\mathrm{Ca_i^{2+}}$ levels were reversibly altered in 35% of the cells (elevated <180 s) and $\mathrm{Ca_i^{2+}}$ was elevated >180 s in the remaining 65% of these cells. These small and resealing pores never caused a clustered pattern of $\mathrm{Ca_i^{2+}}$. However, when pores were large (high PI uptake) or remained open longer than 120 s, the $\mathrm{Ca_i^{2+}}$ levels were mainly irreversibly altered, as $\mathrm{Ca_i^{2+}}$ either remained elevated >180 s (39%) or clustered (52%) (Supplementary Fig. S6, online only). Because large pores with low resealing capabilities cause the most severe damage to a cell, the ratio of the obtained pore size to the resealing coefficient was used as a measure for pore damage. The pore damage was significantly higher for $\mathrm{Ca_i^{2+}}$ fluctuations that clustered than for those that remained elevated >180 s (Fig. 3b). Additionally, the pore damage was significantly higher for both these irreversible $\mathrm{Ca_i^{2+}}$ fluctuations (>180 s or clusters) than for those that returned to equilibrium <180 s (Fig. 3b).

The microbubble oscillation amplitude, obtained from the Brandaris 128 ultra-high-speed recordings, ranged from 0.12−2.65 μm upon insonification from 100−400 kPa (Supplementary Fig. S7, online only). This was predominantly stable cavitation, as only 1 of 108 microbubbles exceeded the threshold for inertial cavitation (*i.e.,* expansion of at least twice its size during oscillation) (Leighton 1994). Sonoporation was induced with microbubble oscillation amplitudes >0.75 μm (n = 77, Supplementary Fig. S7). As illustrated in Figure 3c, a higher microbubble oscillation amplitude >1 μm was needed to irreversibly alter the $\mathrm{Ca_i^{2+}}$ concentration (*i.e.,* when it was elevated for more than 180 s or resulted in clustering). This was significantly larger than the oscillation amplitude required to reversibly alter the $\mathrm{Ca_i^{2+}}$, that is, when it returned to the initial concentration within 180 s.

Opening of cell−cell contacts

In 46% of the fields of view, the oscillating microbubble also induced opening of cell−cell contacts between the cell to which the microbubble was bound and its neighbors. The number of cells in which cell−cell contact opening was observed was significantly higher when the $\mathrm{Ca_i^{2+}}$ fluctuation in the sonoporated cell was elevated >180 s, and even higher when $\mathrm{Ca_i^{2+}}$ clustered (Fig. 3d). Opening of cell−cell contacts did not correlate with the amplitude of the microbubble oscillation (Supplementary Fig. S7). Ultrasound only, without microbubbles, did not enhance opening of cell−cell contacts, as

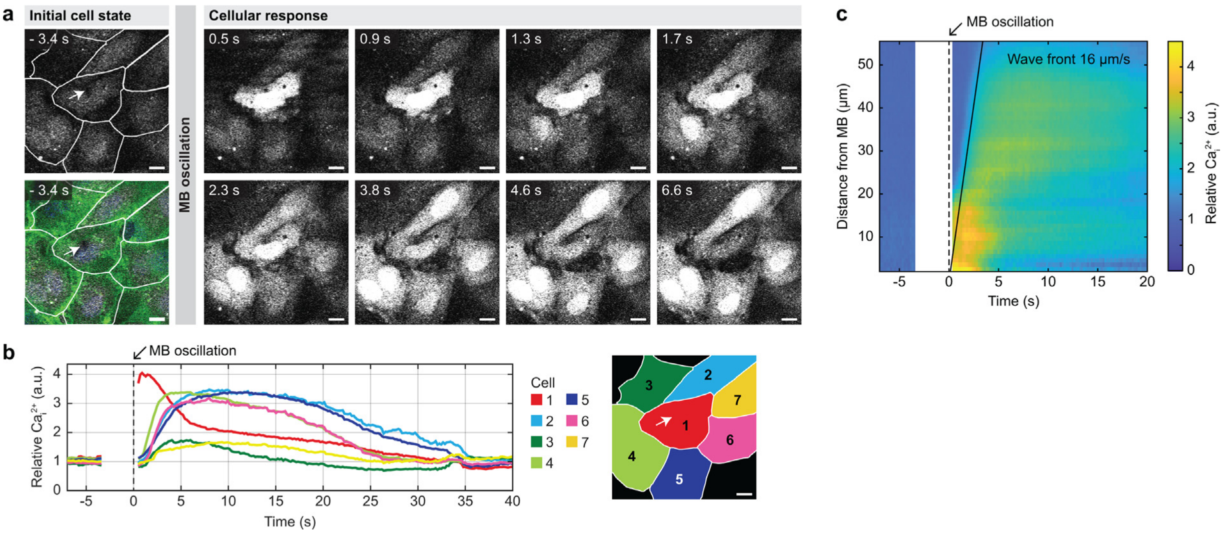

Fig. 4. Calcium wave to all adjacent cells caused by sonoporation resulting from an oscillating microbubble (MB). (a) Selected confocal microscopy frames of intracellular calcium ($\mathrm{Ca_i^{2+}}$) stained with Fluo-4, corresponding to Figure 2c. The initial cell state indicates the microbubble location (*arrow*) and cell delineation. The microbubble was insonified at 0 s. Bars = 10 μm. (b) Mean $\mathrm{Ca_i^{2+}}$ level in each delineated cell relative to the initial equilibrium state before MB oscillation. As all adjacent cells exhibited a $\mathrm{Ca_i^{2+}}$ fluctuation, 100% of the cells were affected. (c) Resulting space−time diagram of the calcium wave. The relative $\mathrm{Ca_i^{2+}}$ level (*i.e.,* normalized to that before ultrasound) is plotted as a function of time and the radial distance from the microbubble. The calcium wavefront (*black solid line*) propagated with a speed of 16 μm/s.

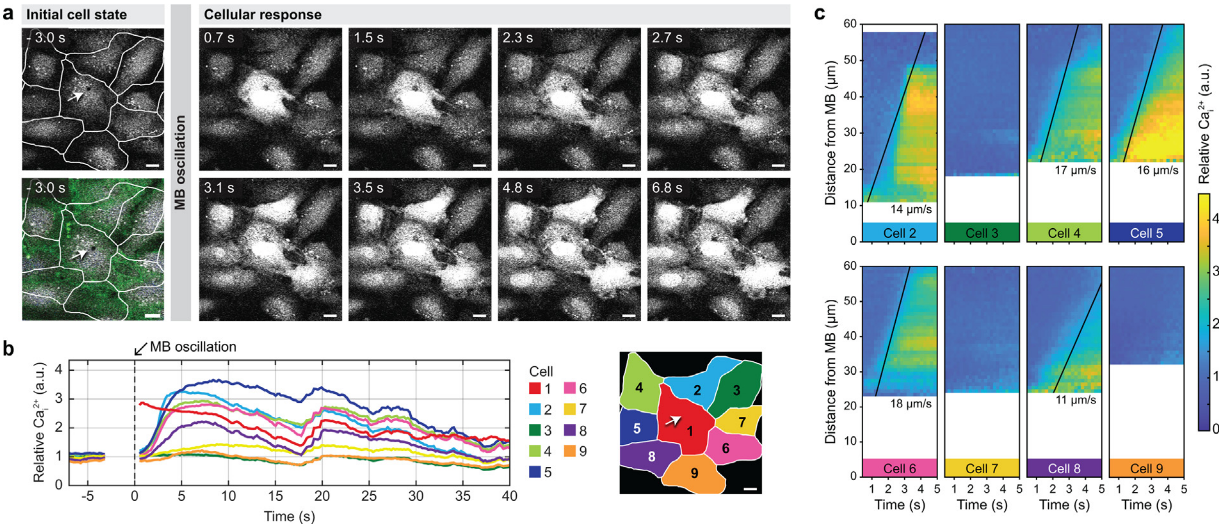

Fig. 5. Calcium wave to only a fraction of the adjacent cells caused by sonoporation resulting from an oscillating microbubble (MB). (a) Selected confocal microscopy frames of intracellular calcium (Ca_i^{2+}) stained with Fluo-4. The initial cell state indicates the microbubble location (*arrow*) and cell delineation. The microbubble was insonified at 0 s. Bars = 10 μm. (b) Mean Ca_i^{2+} level in each delineated cell relative to the initial equilibrium state before MB oscillation. As five of eight adjacent cells exhibited a Ca_i^{2+} fluctuation, 63% of the cells were affected. (c) Resulting space−time diagram of the calcium wave in each adjacent cell. The relative Ca_i^{2+} level (*i.e.,* normalized to that before ultrasound) is plotted as a function of time and the radial distance from the microbubble. The calcium wavefront (*black solid line*) propagated with a median speed of 16 μm/s.

that occurred as often in ultrasound-only as in sham control experiments without ultrasound (7 of 36 cells for sham, 8 of 44 cells for ultrasound only).

Calcium waves

Upon a Ca_i^{2+} fluctuation in the sonoporated cell, an increase in the Ca_i^{2+} concentration was seen to spatially propagate from the sonoporated cell toward adjacent cells (Figs. 4a and 5a). This phenomenon is known as a calcium wave propagating outward from the microbubble location. By monitoring the Fluo-4 intensity in the adjacent cells, the time profiles revealed a delayed increase in Ca_i^{2+}, about 2 s after microbubble oscillation (Figs. 4b and 5b). The increase in Ca_i^{2+} in the adjacent cells was reversible, as it always returned to the equilibrium level within 180 s, independent of the temporal evolution of the Ca_i^{2+} fluctuation in the sonoporated cell. Not all adjacent cells were equally affected in a calcium wave; some cells had a more delayed response and others were not affected at all. Figure 4a illustrates selected frames of confocal microscopy time-lapse imaging of a calcium wave that affected 100% of the adjacent cells, as delayed Ca_i^{2+} fluctuations were observed in all cells (Fluo-4 time profiles in Fig. 4b). Figure 5a illustrates an example of a calcium wave that affected only a fraction (63%) of the adjacent cells, as delayed Ca_i^{2+} fluctuations were observed in 5 of 8 cells (Fluo-4 time profiles in Fig. 5b). When Ca_i^{2+} clustered in the sonoporated cell, it resulted in a calcium wave propagating to more than half of the adjacent cells in 94% of cases (Fig. 6a). When the severity of the Ca_i^{2+} fluctuation in the sonoporated cell decreased, fewer adjacent cells were affected. Additionally, the fraction of affected cells

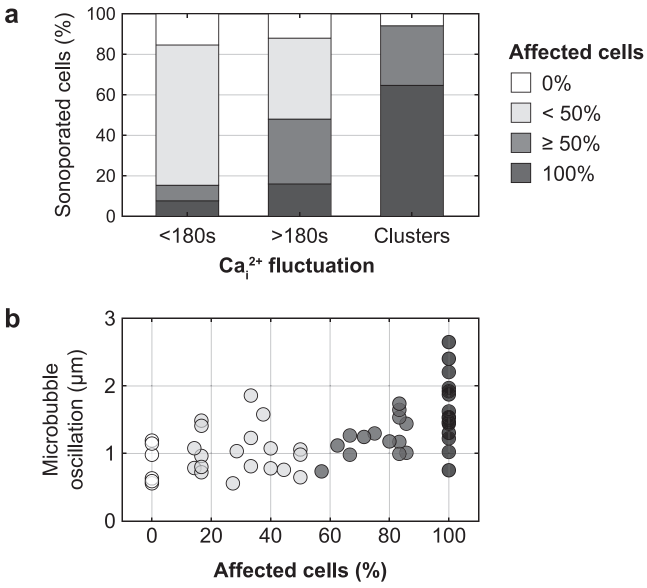

Fig. 6. Fraction of adjacent cells affected in a calcium wave. (a) Fraction of affected cells in a calcium wave induced by each of the distinct Ca_i^{2+} fluctuations in the sonoporated cell. (b) Microbubble oscillation amplitude as a function of the fraction of affected cells in a calcium wave.

during a calcium wave positively correlated with the microbubble oscillation amplitude (Spearman correlation coefficient $\rho = 0.6$, $p < 0.001$; Fig. 6b).

The calcium wavefront, when 100% of the adjacent cells were affected, propagated with a median speed of 15 μm/s (interquartile range: 12−19 μm/s, n = 16; Fig. 4c). When calcium wave propagation is considered as a spherical wave, we assume the full field of view is affected. However, when only a fraction of the adjacent cells exhibit an increase in Ca_i^{2+}, the cells in which Ca_i^{2+} remains stable will interfere with adequate quantification of the wavefront speed. Therefore, to additionally determine the speed of the intracellular calcium wave, the wavefront speed was also quantified within each adjacent cell. The intracellular calcium wavefront propagated with a median speed of 12 μm/s (interquartile range: 8−17 μm/s, n = 191; Fig. 5c). That the intracellular wave speed exhibited only a very weak correlation with the fraction of affected cells (Spearman correlation coefficient $\rho = 0.3$, $p < 0.001$) suggests that the intracellular wavefront speed was independent of the number of cells affected. Finally, there was no statistically significant difference between the propagation speed computed either over the full field of view or within each adjacent cell, that is, between the intercellular and the intracellular calcium wave propagation speeds.

DISCUSSION

The microbubble−cell interaction necessary for sonoporation, Ca_i^{2+} fluctuations, propagation of calcium waves and opening of cell−cell contacts was unraveled using the combined Brandaris 128 ultra-high-speed camera and confocal microscope.

By studying the microbubble−cell interaction at ultra-high temporal and high spatial resolution, we found that a microbubble oscillation amplitude >0.75 μm was needed to induce sonoporation in endothelial cells. This threshold for a 10-cycle pulse is in the range of >0.72 μm for a 16-cycle pulse or >1.02 μm for an 8-cycle pulse, as previously reported for 2 MHz (Helfield et al. 2016). In addition, our study found that sonoporation always resulted in an immediate Ca_i^{2+} influx through the created membrane pore, as was also found for rat cardiomyoblasts (Fan et al. 2010). We found that the highest pore damage (large pore size and poor membrane resealing) resulted in the most severe Ca_i^{2+} fluctuations, which also strongly correlated with the microbubble oscillation amplitude. The Ca_i^{2+} fluctuation was reversible (*i.e.,* elevated <180 s) for oscillation amplitudes <1 μm, indicating that the cell membrane resealed and normal homeostatic Ca_i^{2+} concentrations were restored. This reversibility suggests cell viability after sonoporation (Fan et al. 2010). Reversible Ca_i^{2+} fluctuations have previously been reported in the literature, but the necessary microbubble oscillation behavior was never resolved (Juffermans et al. 2006, 2009; Kumon et al. 2007, 2009; Meijering et al. 2009; Fan et al. 2010; Park et al. 2011). Our results suggest that there is a very narrow band of microbubble oscillation amplitudes, from >0.75 to <1 μm, in which cell viability is maintained upon sonoporation. However, it remains to be investigated if the reversible Ca_i^{2+} fluctuation that suggests cell viability in the short term cannot trigger long-term cellular responses that, for instance, interfere in cell proliferation or induce DNA damage (Berridge et al. 2000; Honda et al. 2004; Hassan et al. 2010).

With microbubble oscillation amplitudes >1 μm, we observed an irreversible alteration of the Ca_i^{2+} concentration, as Ca_i^{2+} either remained elevated >180 s or clustered. Ca_i^{2+} fluctuations that remain elevated >180 s have also been reported in Chinese hamster ovary cells treated with oscillating microbubbles, and were assumed to be caused by unsuccessful membrane resealing (Kumon et al. 2007, 2009). However, in the experimental procedure used in these studies by Kumon et al., pore formation was not evaluated to support this hypothesis. In our study, pore formation and resealing were assessed based on PI influx. We observed that even when the pore created upon sonoporation was small and resealed within 120 s (low PI uptake), about 65% of the cells exhibited irreversible Ca_i^{2+} fluctuations that remained elevated >180 s (Supplementary Fig. S6, online only). Therefore, when Ca_i^{2+} remains elevated, it does not necessarily mean sustained membrane damage occurred, but it does indicate the cell is not able to regain homeostatic concentrations after the Ca_i^{2+} overload. Because a highly toxic overload of Ca_i^{2+} can still trigger the onset of biological responses that result in cell death (Berridge et al. 2000), we hypothesize that Ca_i^{2+} levels that are elevated >180 s are indicative of irreversible cell damage, despite membrane resealing. In other words, membrane resealing is required but not sufficient to preserve cell viability. For the first time, clustering of Ca_i^{2+} was observed upon sonoporation. This characteristic uptake pattern is likely owing to Ca_i^{2+} compartmentalization into cellular organelles that function as Ca_i^{2+} stores (Thomas et al. 2000), such as the endoplasmic reticulum (ER) and mitochondria, and efflux of free Ca_i^{2+} while the pore remains open. It is known that an overload of Ca_i^{2+} will accumulate in the mitochondria which can trigger apoptosis (Nicotera and Orrenius 1998; Orrenius et al. 2003). A flow cytometry study on leukemia cells revealed that oscillating microbubbles can indeed trigger this Ca_i^{2+}-dependent apoptotic pathway (Honda et al. 2004; Hassan et al. 2010). Since Ca_i^{2+} clustering occurred for the highest pore damage coefficients, it is indicative of excessive trauma, which might also directly lead to necrosis (Hassan et al. 2010). A granular-like fluorescence has previously been reported when imaging an oxidation-sensitive fluorescent probe (2′,7′-dichlorofluorescein) to study the effect of oscillating microbubbles on reactive oxygen species (ROS). It was suggested that this apparent granulation was caused by high levels of ROS in the mitochondria related to the Ca_i^{2+} influx (Jia et al. 2018).

The Ca_i^{2+} fluctuations spatially propagated within each cell via intracellular calcium waves and among neighboring cells via intercellular calcium waves. These are complex spatiotemporal processes regulated by cellular signaling mechanisms and limited by passive diffusion (Leybaert and Sanderson 2012). Intracellular calcium propagation induced by an oscillating microbubble occurs through two main mechanisms. First, upon pore formation, external calcium ions diffuse into the cytosol and can trigger a calcium-induced release of Ca_i^{2+} from the ER (Berridge et al. 2000). Second, membrane stress and elevated Ca_i^{2+} levels trigger the production of inositol 1,4,5-trisphosphate (IP3), which diffuses through the cell and also stimulates Ca_i^{2+} release from the ER (Leybaert and Sanderson 2012). At the same time, the intercellular calcium wave leads to a Ca_i^{2+} rise in adjacent cells. However, it is not directly the Ca_i^{2+} that diffuses among cells but the IP3 messenger, as described in detail by Leybaert and Sanderson (2012). Elevated IP3 levels will be transmitted to adjacent cells through gap junctions or through paracrine signaling, by stimulating adenosine triphosphate (ATP) release into the extracellular space, which in turn stimulates the production of IP3. Both of these processes result in elevated IP3 levels in adjacent cells, which will stimulate Ca_i^{2+} release from the ER, leading to the observed delayed Ca_i^{2+} fluctuations. In our study, some adjacent cells were not affected by the induced calcium wave, suggesting that there were fewer gap junctions for IP3 transmission or fewer receptors on the cell membrane sensitive to the increase in extracellular ATP to stimulate IP3 production. Additionally, we found that larger microbubble oscillation amplitudes caused a calcium wave that affected more adjacent cells. This is likely owing to the creation of a larger pore and, hence, a more severe Ca_i^{2+} fluctuation that causes a higher production of IP3, so more internal messenger is available to trigger the subsequent pathways for calcium wave propagation. In our study, we used Fluo-4 to quantify the relative changes in Ca_i^{2+} using a single imaging channel and normalizing to the initial Ca_i^{2+} levels in each cell. To quantitively compare the Ca_i^{2+} levels between cells, ideally a dual-wavelength ratiometric calcium indicator such as Fura-2 should be used (Bootman et al. 2013). However, for ratiometric dyes, two imaging channels are required. As only four simultaneous imaging channels are available in the confocal microscope, either the nuclei, cell membrane or uptake of PI could not have been imaged if a ratiometric calcium dye had been used.

The high spatial and temporal resolution of the confocal microscope allowed us to quantify the spatiotemporal evolution of calcium waves as a spherical wave. The intracellular calcium wavefront propagated at ~12 μm/s, independent of how many cells were affected, and the intercellular wave front propagated at ~15 μm/s when all adjacent cells were affected. These calcium wave speeds are in agreement with the ~10–20 μm/s generally reported in the literature for various stimuli and cell types (Leybaert and Sanderson 2012), the 17 μm/s estimated in endothelial cells upon force probe stimulation (Long et al. 2012) and the 7–20 μm/s in Chinese hamster ovary cells upon oscillating microbubbles (Kumon et al. 2009).

Opening of cell–cell contacts was observed upon an oscillating microbubble, causing gap formation between neighboring cells by the disruption of intercellular junctions. This is a clinically relevant therapeutic bio-effect because it can facilitate the extravasation of drug compounds from the vasculature, for instance, to overcome the blood–brain barrier (Konofagou 2012). The occurrence of opening of cell–cell contacts was not predictable from microbubble oscillation amplitude. However, it did strongly correlate to the severity of the induced Ca_i^{2+} fluctuation. When an irreversible Ca_i^{2+} fluctuation was induced upon sonoporation, there was a significantly higher chance of cell–cell contact opening between the cell and its neighbors. This suggests that cell–cell contact opening is a biological response triggered by elevated Ca_i^{2+} levels. Membrane stress and elevated Ca_i^{2+} can cause rearrangement of the cytoskeleton, which coupled to the tight junctions might be causing the opening of cell–cell contacts (Hassan et al. 2010; Li et al. 2018). Rearrangement of the cytoskeleton because of an oscillating microbubble has been reported (Chen et al. 2014), but it remains to be evaluated if this is associated with an increased occurrence of cell–cell contact opening. Additionally, a rise in Ca_i^{2+} can cause endothelial cell contraction and thereby reduce the cell surface area (Mehta and Malik 2006). This might facilitate quicker resealing of the pore by reducing the pore area and making membrane lipids available to repair the pore. We observed that upon opening of cell–cell contacts, the intercellular gaps remained open for >210 s. The single example previously reported in the literature indicated that cell–cell contacts can remain open for tens of minutes (Helfield et al. 2016). However, they did not correlate this bio-effect to microbubble behavior, sonoporation or Ca_i^{2+} fluctuations. It remains to be investigated how the long-term recovery of cell−cell contacts correlates to the Ca_i^{2+} fluctuation and calcium wave.

CONCLUSIONS

Using the combined Brandaris 128 ultra-high-speed camera and confocal microscope, we could simultaneously resolve specific microbubble oscillation, sonoporation, Ca_i^{2+} fluctuations, propagation of calcium waves and opening of cell−cell contacts. Three distinct Ca_i^{2+} uptake profiles were identified upon sonoporation, which propagated to adjacent cells via calcium waves. The distinct Ca_i^{2+} fluctuations strongly correlated with the microbubble oscillation amplitude, the severity of pore damage induced by sonoporation, the occurrence of cell−cell contact opening and the number of adjacent cells affected in a calcium wave. This novel optical imaging system yields new insights into the microbubble−cell interaction to aid the development of microbubble-enhanced drug delivery.

Acknowledgments—We thank S. A. G. Langeveld from the Department of Biomedical Engineering, Erasmus University Medical Center Rotterdam, for assistance with microbubble preparation and M. Manten and G. Springeling from the Department of Experimental Medical Instrumentation, Erasmus University Medical Center Rotterdam, for technical assistance. The authors also thank R. Verduyn Lunel, E. Verver and A. Scarpellini from Nikon Instruments Europe for their contribution to development of the optical imaging system. This research was supported by the Applied and Engineering Sciences TTW (Veniproject 13669), part of the Netherlands Organization for Scientific Research (NWO).

Conflict ofinterest disclosure—The authors declare no conflict of interest.

SUPPLEMENTARY MATERIALS

Supplementary material associated with this article can be found in the online version at doi:10.1016/j.ultrasmedbio.2020.03.029.

REFERENCES

Bao S, Thrall BD, Miller DL. Transfection of a reporter plasmid into cultured cells by sonoporation in vitro. Ultrasound Med Biol 1997;23:953–959.

Beekers I, Lattwein KR, Kouijzer JJ, Langeveld SA, Vegter M, Beurskens R, Mastik F, Verduyn Lunel R, Verver E, van der Steen AF, de Jong N, Kooiman K. Combined confocal microscope and Brandaris 128 ultra-high-speed camera. Ultrasound Med Biol 2019a;45:2575–2582.

Beekers I, van Rooij T, van der Steen AFW, de Jong N, Verweij MD, Kooiman K. Acoustic Characterization of the CLINIcell for ultrasound contrast agent studies. IEEE Trans Ultrason Ferroelectr Freq Control 2019b;66:244–246.

Berridge MJ, Lipp P, Bootman MD. The versatility and universality of calcium signalling. Nat Rev Mol Cell Biol 2000;1:11–21.

Bootman MD, Rietdorf K, Collins T, Walker S, Sanderson M. Ca^{2+}-sensitive fluorescent dyes and intracellular Ca^{2+} imaging. Cold Spring Harbor Protoc 2013;8:83–99.

Carafoli E, Krebs J. Why calcium? How calcium became the best communicator. J Biol Chem 2016;291:20849–20857.

Chen X, Wang J, Versluis M, de Jong N, Villanueva FS. Ultra-fast bright field and fluorescence imaging of the dynamics of micrometer-sized objects. Rev Sci Instrum 2013;84 063701.

Chen X, Leow RS, Hu Y, Wan JMF, Yu ACH. Single-site sonoporation disrupts actin cytoskeleton organization. J R Soc Interface 2014;11 20140071.

Chin CT, Lanćee C, Borsboom J, Mastik F, Frijlink ME, de Jong N, Versluis M, Lohse D. Brandaris 128: A digital 25 million frames per second camera with 128 highly sensitive frames. Rev Sci Instrum 2003;74:5026–5034.

Deng CX, Sieling F, Pan H, Cui J. Ultrasound-induced cell membrane porosity. Ultrasound Med Biol 2004;30:519–526.

Edidin M. A rapid, quantitative fluorescence assay for cell damage by cytotoxic antibodies. J Immunol 1970;104:1303–1306.

Fan Z, Kumon RE, Park J, Deng CX. Intracellular delivery and calcium transients generated in sonoporation facilitated by microbubbles. J Control Release 2010;142:31–39.

Fan Z, Liu H, Mayer M, Deng CX. Spatiotemporally controlled single cell sonoporation. Proc Natl Acad Sci 2012;109:16486–16491.

Hassan MA, Campbell P, Kondo T. The role of Ca^{2+} in ultrasound-elicited bioeffects: Progress, perspectives and prospects. Drug Discov Today 2010;15:892–906.

Helfield B, Chen X, Watkins SC, Villanueva FS. Biophysical insight into mechanisms of sonoporation. Proc Natl Acad Sci 2016;113:9983–9988.

Honda H, Kondo T, Zhao QL, Feril LB, Kitagawa H. Role of intracellular calcium ions and reactive oxygen species in apoptosis induced by ultrasound. Ultrasound Med Biol 2004;30:683–692.

Jia C, Xu L, Han T, Cai P, Yu AC, Qin P. Generation of reactive oxygen species in heterogeneously sonoporated cells by microbubbles with single-pulse ultrasound. Ultrasound Med Biol 2018;44:1074–1085.

Juang EK, De Cock I, Keravnou C, Gallagher MK, Keller SB, Zheng Y, Averkiou M. Engineered 3D microvascular networks for the study of ultrasound-microbubble-mediated drug delivery. Langmuir 2019;35:10128–10138.

Juffermans LJ, Dijkmans PA, Musters RJ, Visser CA, Kamp O. Transient permeabilization of cell membranes by ultrasound-exposed microbubbles is related to formation of hydrogen peroxide. Am J Physiol Heart Circ Physiol 2006;291:H1595–H1601.

Juffermans LJM, van Dijk A, Jongenelen CAM, Drukarch B, Reijerkerk A, de Vries HE, Kamp O, Musters RJP. Ultrasound and microbubble-induced intra- and intercellular bioeffects in primary endothelial cells. Ultrasound Med Biol 2009;35:1917–1927.

Klibanov AL, Rasche PT, Hughes MS, Wojdyla JK, Galen KP, Wible JH, Brandenburger GH. Detection of individual microbubbles of ultrasound contrast agents: Imaging of free-floating and targeted bubbles. Invest Radiol 2004;39:187–195.

Konofagou EE. Optimization of the ultrasound-induced blood−brain barrier opening. Theranostics 2012;2:1223–1237.

Kooiman K, Vos HJ, Versluis M, de Jong N. Acoustic behavior of microbubbles and implications for drug delivery. Adv Drug Deliv Rev 2014;72:28–48.

Kumon RE, Aehle M, Sabens D, Parikh P, Kourennyi D, Deng CX. Ultrasound-induced calcium oscillations and waves in Chinese hamster ovary cells in the presence of microbubbles. Biophys J 2007;93:L29–L31.

Kumon RE, Aehle M, Sabens D, Parikh P, Han YW, Kourennyi D, Deng CX. Spatiotemporal effects of sonoporation measured by real-time calcium imaging. Ultrasound Med Biol 2009;35:494–506.

Leighton TG. The acoustic bubble. London: Academic Press; 1994.

Lentacker I, De Cock I, Deckers R, De Smedt SC, Moonen CT. Understanding ultrasound induced sonoporation: Definitions and underlying mechanisms. Adv Drug Deliv Rev 2014;72:49–64.

Leybaert L, Sanderson MJ. Intercellular Ca Waves: Mechanisms and function. Physiol Review 2012;92:1359–1392.

Li F, Yang C, Yuan F, Liao D, Li T, Guilak F, Zhong P. Dynamics and mechanisms of intracellular calcium waves elicited by tandem bubble-induced jetting ow. Proc Natl Acad Sci USA 2018;115:E353–E362.

Lindner JR, Song J, Christiansen J, Klibanov AL, Xu F, Ley K. Ultrasound assessment of inflammation and renal tissue injury with microbubbles targeted to P-selectin. Circulation 2001;104:2107–2112.

Long J, Junkin M, Wong PK, Hoying J, Deymier P. Calcium wave propagation in networks of endothelial cells: Model-based theoretical and experimental study. PLoS Comput Biol 2012;8 e1002847.

Mehta D, Malik AB. Signaling mechanisms regulating endothelial permeability. Physiol Rev 2006;86:279–367.

Meijering BDM, Juffermans LJM, van Wamel A, Henning RH, Zuhorn IS, Emmer M, Versteilen AMG, Paulus WJ, van Gilst WH, Kooiman K, de Jong N, Musters RJ, Deelman LE, Kamp O. Ultrasound and microbubble-targeted delivery of macromolecules is regulated by induction of endocytosis and pore formation. Circ Res 2009;104:679–687.

Miller DL, Bao S, Morris JE. Sonoporation of cultured cells in the rotating tube exposure system. Ultrasound Med Biol 1999;25:143–149.

Mullick Chowdhury S, Lee T, Willmann JK. Ultrasound-guided drug delivery in cancer. Ultrasonography 2017;36:171–184.

Neuwelt E, Abbott NJ, Abrey L, Banks WA, Blakley B, Davis T, Engelhardt B, Grammas P, Nedergaard M, Nutt J, Pardridge W, Rosenberg GA, Smith Q, Drewes LR. Strategies to advance translational research into brain barriers. Lancet Neurol 2008;7:84–96.

Nicotera P, Orrenius S. The role of calcium in apoptosis. Cell Calcium 1998;23:173–180.

Orrenius S, Zhivotovsky B, Nicotera P. Regulation of cell death: The calcium−apoptosis link. Nat Rev Mol Cell Biol 2003;4:552–565.

Park J, Fan Z, Deng CX. Effects of shear stress cultivation on cell membrane disruption and intracellular calcium concentration in sonoporation of endothelial cells. J Biomech 2011;44:164–169.

Qin D, Zhang L, Chang N, Ni P, Zong Y, Bouakaz A, Wan M, Feng Y. In situ observation of single cell response to acoustic droplet vaporization: Membrane deformation, permeabilization, and blebbing. Ultrason Sonochem 2018a;47:141–150.

Qin P, Han T, Yu AC, Xu L. Mechanistic understanding the bioeffects of ultrasound-driven microbubbles to enhance macromolecule delivery. J Control Release 2018b;272:169–181.

Roovers S, Segers T, Lajoinie G, Deprez J, Versluis M, De Smedt SC, Lentacker I. The role of ultrasound-driven microbubble dynamics in drug delivery: From microbubble fundamentals to clinical translation. Langmuir 2019;35:10173–10191.

Shamout FE, Pouliopoulos AN, Lee P, Bonaccorsi S, Towhidi L, Krams R, Choi JJ. Enhancement of non-invasive trans-membrane drug delivery using ultrasound and microbubbles during physiologically relevant flow. Ultrasound Med Biol 2015;41:2435–2448.

Sutton JT, Haworth KJ, Pyne-Geithman G, Holland CK. Ultrasound-mediated drug delivery for cardiovascular disease. Expert Opin Drug Deliv 2013;10:573–592.

Thomas D, Tovey SC, Collins TJ, Bootman MD, Berridge MJ, Lipp P. A comparison of fluorescent Ca^{2+} indicator properties and their use in measuring elementary and global Ca^{2+} signals. Cell Calcium 2000;28:213–223.

van der Meer SM, Dollet B, Voormolen MM, Chin CT, Bouakaz A, de Jong N, Versluis M, Lohse D. Microbubble spectroscopy of ultrasound contrast agents. J Acoust Soc Am 2007;121:648–656.

van Rooij T, Skachkov I, Beekers I, Lattwein KR, Voorneveld JD, Kokhuis TJ, Bera D, Luan Y, van der Steen AF, de Jong N, Kooiman K. Viability of endothelial cells after ultrasound-mediated sonoporation: Influence of targeting, oscillation, and displacement of microbubbles. J Control Release 2016;238:197–211.

van Wamel A, Kooiman K, Harteveld M, Emmer M, ten Cate FJ, Versluis M, de Jong N. Vibrating microbubbles poking individual cells: Drug transfer into cells via sonoporation. J Control Release 2006;112:149–155.

Wang M, Zhang Y, Cai C, Tu J, Guo X, Zhang D. Sonoporation-induced cell membrane permeabilization and cytoskeleton disassembly at varied acoustic and microbubble-cell parameters. Sci Rep 2018;8:3885.

Wu J, Nyborg WL. Ultrasound, cavitation bubbles and their interaction with cells. Adv Drug Deliv Rev 2008;60:1103–1116.

Yang C, Li Y, Du M, Chen Z. Recent advances in ultrasound-triggered therapy. J Drug Target 2019;27:33–50.